Accepted Manuscript

Three-dimensional micromechanical assessment of bio-inspired composites with non-uniformly dispersed inclusions

Aram Bahmani, Geng Li, Thomas L. Willett, John Montesano

Please cite this article as: Bahmani, A., Li, G., Willett, T.L., Montesano, J., Three-dimensional micromechanical assessment of bio-inspired composites with non-uniformly dispersed inclusions, *Composite Structures* (2019), doi: https://doi.org/10.1016/j.compstruct.2019.01.056

Three-dimensional micromechanical assessment of bio-inspired composites with non-uniformly dispersed inclusions

Aram Bahmani [a], Geng Li [a, b], Thomas L. Willett [c], John Montesano [a *]

[a] Department of Mechanical and Mechatronics Engineering, University of Waterloo, 200 University Ave. West, Waterloo, N2L 3G1, Canada.

[b] College of Advanced Interdisciplinary Studies, National University of Defense Technology, 137 Yanwachizhengjie Street, Changsha, Hunan, 410073, China.

[c] Department of Systems Design Engineering, University of Waterloo, 200 University Ave. West, Waterloo, N2L 3G1, Canada.

[*] Corresponding Author: Email address: john.montesano@uwaterloo.ca (J. Montesano)

Abstract

Bio-inspired composites with hexagonal platelet and cylindrical inclusions were studied. A novel algorithm termed staggered hardcore algorithm (SHCA) was used to rapidly generate 3D periodic representative volume elements (RVE) for bio-inspired composites with staggered non-uniformly dispersed inclusions. The spatial dispersions of inclusions in these generated RVEs were assessed using autocorrelation analysis, demonstrating the effectiveness of the SHCA algorithm. Orthotropic elastic properties of two different bio-inspired composites were computed and compared with analytical models, namely modified shear-lag, Mori-Tanaka and Halpin-Tsai, as well as available experimental data from the literature. For lower inclusion volume fractions, the computed results correlated well with experimental data and the analytical results. However, for higher inclusion volume fractions and aspect ratios the analytical results diverged, particularly Mori-Tanaka and modified shear-lag models which was similarly reported in previous studies. The capabilities of the computational model were further demonstrated through a comparative study of orthotropic elastic constants for the cylindrical and hexagonal inclusion composites. The study revealed the necessity to use 3D micromechanical models with realistic inclusion dispersions for accurately assessing the response of high inclusion volume fraction bio-inspired composites.

1. Introduction

In practice, due to a range of distinct engineering applications, a variety of high-performance materials are required to tailor the mechanical response of structures. Many recent studies have reported various biological materials that have been naturally optimized over millions of years and as a result exhibit remarkable mechanical performance, including bone, tooth enamel, mollusk shell, among others [1-4]. These natural composites benefit from simultaneous low density, and high specific toughness, specific stiffness, and specific strength, which are unmatched in comparison to traditional engineering material counterparts. The key features, which are pervasive among the materials mentioned above, are the combination of overlapping, stiff inclusions embedded in a compliant, soft matrix arranged in complex staggered architectures. Staggered microstructure is the main archetype by which bio-inspired composite materials are developed. Various research groups have been motivated to develop and fabricate bio-inspired composites in order to investigate microstructure-property relationships [1-4].

A number of inclusion types, including hexagonal (i.e., flake-like) platelet and rod shaped (i.e., cylindrical), have been utilized to generate bio-inspired composites (see Fig.1) by employing a variety of fabrication methods. Examples of these techniques include doctor blading, 3D printing, magnetically assisted slip casting, hot-press assisted slip casting, among others [1-4]. Characterization of bio-inspired composites with different inclusion shapes and complex microstructural arrangements, and the establishment of general design guidelines, is pivotal for widespread adoption of these materials. To facilitate this, it is essential to develop robust high-fidelity design tools to assess the performance of bio-inspired composites.
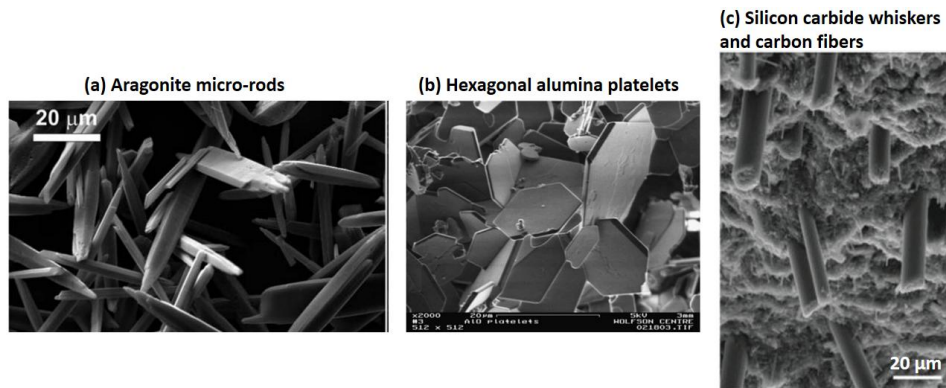
2

Fig.1. Different inclusion shapes used in bio-inspired composites. **(a)** aragonite micro-rods [5], **(b)** hexagonal alumina micro-platelets [6], **(c)** silicon carbide whiskers and carbon fibers [7].

Several analytical solutions have been proposed to investigate the characteristics and properties of various natural and biological composites, such as stiffness, strength, toughness, and interfacial properties [8-10]. However, all of these models were 2D analytical solutions, and the third dimension, which defines inclusion shape and dictates whether plane strain constraint is imposed, has not been considered. In addition, analytical models often cannot account for the complexities of bio-inspired composite microstructures, such as non-uniform inclusion distributions.

Micromechanical finite element (FE) modeling provides an efficient means to conduct virtual experiments for various material systems during design, while at the same time allowing for greater flexibility with regards to assessing material nonlinearities and local damage progression of bio-inspired composites. A representative volume element (RVE) which accurately depicts a material's microstructure is employed to evaluate its response under various loading conditions. Mirkhalaf and Barthelat [11] developed a 2D RVE to assess the longitudinal performance of nacre-mimetic composites. Recently, Mirkhalaf and Ashrafi [12] proposed 2D RVEs to explore the effects of voids on the mechanical performance of staggered microstructures. During the past decade, Barthelat and coworkers [13-15] have proposed 2D and 3D RVEs to characterize the

3

interfaces and junctions of the nacreous layer from mollusk shells. These studies have made notable contributions; however, most proposed FE models for biological or bio-inspired composites utilized 2D RVEs, the limitations of which include the inability to assess out-of-plane mechanical properties or 3D damage evolution under realistic and practical multiaxial stress states. Although several 3D FE micromechanical models have been proposed to characterize various staggered and aligned discontinuous inclusion-reinforced composites, overall microstructure, inclusion shape, and boundary conditions are often simplified and not an accurate representation of the material. Also, complicated algorithms are often employed to generate 3D RVE geometries, mesh schemes, and apply periodic boundary conditions [16-21]. In addition, the influences of various inclusion shapes and aspect ratios under different stress states have not been broadly compared using micromechanical FE models. Hence, to accurately assess the local damage evolution or 3D mechanical properties of bio-inspired materials, 3D RVEs with staggered or aligned microstructures consisting of non-uniformly dispersed inclusions with various shapes are required. This is challenging, particularly if periodic geometries and boundary conditions are required.

The main goal of this study was to develop a new robust FE-based micromechanical tool for assessing the response of high-performance bio-inspired composite materials with relatively high inclusion volume fractions and complex microstructures. First, a novel and efficient algorithm was developed to generate realistic 3D RVEs for various bio-inspired composites containing staggered and aligned inclusions with non-uniform dispersions and high volume fractions, which is challenging at best with existing algorithms or commercial software. The generated RVEs facilitated the application of periodic boundary conditions, while two inclusion shapes, different aspect ratios and volume fractions were considered in the study. To assess the non-uniformity of

4

the RVE inclusion dispersion, a 3D autocorrelation statistical analysis was employed. Furthermore, the generated RVEs for two bio-inspired composites, namely hexagonal platelet and cylindrical inclusion-based, were used to calculate all homogenized orthotropic elastic constants over a range of inclusion volume fractions and aspect ratios, which is useful for calibration of continuum-based constitutive equations. The models were validated using experimental data reported in the literature and compared with established analytical models. The advantages of the proposed model for predicting homogenized properties when compared to existing analytical and computational models was also revealed, in particular for cases with high inclusion volume fractions and aspect ratios. The study demonstrates that the proposed computational tool may be a suitable plug-in with commercial FE software for accurately assessing the mechanical properties of bio-inspired composites, and in the future may be used for predicting and better understanding their complex progressive failure characteristics.

2. Analytical models for discontinuous inclusion-based composites

Established analytical models, including Mori-Tanaka, modified shear lag and Halpin-Tsai, were utilized to calculate the elastic properties for the studied composites and provide a comparison with the generated 3D RVEs. These models are reviewed herein, while relevant predictions are presented in Section 4.

2.1. Mori–Tanaka model

The Mori–Tanaka model can predict the elastic stiffness tensor of a composite material with assumed elliptical inclusions using [12]:

$$C_c = C_m + \varphi_i \left\langle (C_i - C_m) A_i \right\rangle \left[(1 - \varphi_i) I + \varphi_i \left\langle A_i \right\rangle \right]^{-1} \tag{1}$$

5

where C_c, C_m, and C_i are elastic stiffness tensors of the composite, matrix, and inclusion respectively. φ_i is the inclusion volume fraction, I is fourth order unit tensor, and A_i is the dilute mechanical strain concentration tensor which can be expressed as follows:

$$A_i = \left[I + S \left(C_m \right)^{-1} \left(C_i - C_m \right) \right]^{-1} \tag{2}$$

The elements of Eshelby's tensor S are functions of the inclusion aspect ratio (ρ) and the matrix Poisson's ratio (ν_m), which are presented in Table 1 and by Eqs. (3)-(7).

Table.1 Eshelby's tensor elements for elliptical inclusions.

Tensor element	Expression
s_{11}	$4Q/3 + R\,I_3 + 2\rho^2 T$
$s_{22} = s_{33}$	$Q + R\,I_1 + 3T/4$
$s_{23} = s_{32}$	$Q/3 - R\,I_1 + 4T/3$
$s_{21} = s_{31}$	$-RI_1 - \rho^2 T$
$s_{12} = s_{13}$	$-R\,I_3 - T$
s_{44}	$Q/3 - R\,I_1 + T/4$
$s_{55} = s_{66}$	$2R - R\,I_1/2 + (1+\rho^2)\,T/4$
All other s_{ij}	0

$$I_1 = \frac{2\rho}{\sqrt{\left(\rho^2-1\right)^3}} \left(\rho\sqrt{\rho^2-1} - \cosh^{-1}(\rho) \right) \tag{3}$$

$$Q = \frac{3}{8(1-\nu_m)} \tag{4}$$

$$R = \frac{1 - 2\nu_m}{8(1 - \nu_m)} \tag{5}$$

$$T = Q\frac{4 - 3I_1}{3(\rho^2 - 1)} \tag{6}$$

$$I_3 = 4 - 2I_1 \tag{7}$$

2.2. Modified shear lag

Another well-known analytical model for discontinuous composites is the shear lag model, of which many versions have been developed [8-10, 22]. A modified shear lag model is employed herein to predict longitudinal modulus (E_1) of aligned discontinuous composites using the following:

$$E_1 = E_i\varphi_i\left[1 - \frac{(E_i - E_m)\tanh\left(\frac{1}{h}\left[\frac{2E_m}{E_i(1+\varphi_m)\ln\left(\frac{1}{\varphi_i}\right)}\right]^{0.5}\right)}{E_i\left(\frac{1}{h}\left[\frac{2E_m}{E_i(1+\varphi_m)\ln\left(\frac{1}{\varphi_i}\right)}\right]^{0.5}\right)}\right] + E_m(1 - \varphi_i) \tag{8}$$

where E_i and E_m represent Young's modulus of inclusion and matrix respectively, φ_i and φ_m denote inclusion and matrix volume fraction respectively, and l is the length of cylindrical inclusions or diameter of hexagonal inclusions (see Fig.5). Moreover, h is the diameter of cylindrical inclusions or the thickness of hexagonal inclusions.

2.3. Halpin-Tsai model

Another well-known model used to predict the longitudinal Young's modulus of discontinuous composites is the Halpin-Tsai model, which is defined as follows [22]:

$$E_1 = E_m \left[\cfrac{1 + \left(\frac{2l}{h} \right) \left(\cfrac{\left(\frac{E_i}{E_m} \right) - 1}{\left(\frac{E_i}{E_m} \right) + \frac{2l}{h}} \right) \varphi_i}{1 - \left(\cfrac{\left(\frac{E_i}{E_m} \right) - 1}{\left(\frac{E_i}{E_m} \right) + \frac{2l}{h}} \right) \varphi_i} \right] \tag{9}$$

This model also is used to predict and compare the Young's modulus of discontinuous composites with other analytical models and finite element micromechanical models.

3. RVE generation and micromechanical finite element modeling

3.1. 3D staggered hard-core algorithm (SHCA)

One of the main challenges in modeling multi-inclusion 3D RVEs is to efficaciously generate non-uniformly dispersed inclusion geometries. In this regard, several algorithms have been developed including the hard-core random dispersion algorithm (HCRDA) and its variants [23]. Due to jamming limitations, these algorithms are not efficient in generating periodic 3D RVEs with non-uniformly dispersed staggered inclusions at high volume fractions. Other established algorithms including the nearest neighbor algorithm (NNA), the modified NNA (MNNA), and the elastic collision algorithm (ECA) have similar shortcomings [23-31]. These, along with other algorithms, [20, 32-37] have additional shortcomings including an inability to converge at high inclusion volume fractions, being limited to the generation of 2D RVEs with simplified inclusion shapes, being inappropriate for composites with discontinuous inclusions, being too complex to implement or not easily linkable to commercial FE software, or requiring significant time to converge.

In order to overcome these limitations, a new random algorithm, called the 3D Staggered Hard-Core algorithm (SHCA), was developed in this study. It is written based on the well-known

8

Hard-Core model. In the primary hard-core model, random particle dispersions are generated through a spherical core, and the RVEs have non-periodic and non-staggered morphology. However, our 3D SHCA can generate periodic RVEs with hexagonal or cylindrical particles having various aspect ratios in a non-uniformly staggered scheme. This rapid algorithm is simple to use and flexible for generating the coordinates and the geometry of different inclusion shapes and volume fractions. Hence, this three-dimensional algorithm is notably novel and useful, particularly in the field of biomimetic and bio-inspired composite materials.

The 3D SHCA depicted as a flowchart in Fig. 2 was implemented into a MATLAB code for generating RVEs with inclusion volume fractions up to 40%. This volume fraction is remarkably high for 3D discontinuous staggered and aligned inclusion-reinforced bio-inspired composites.
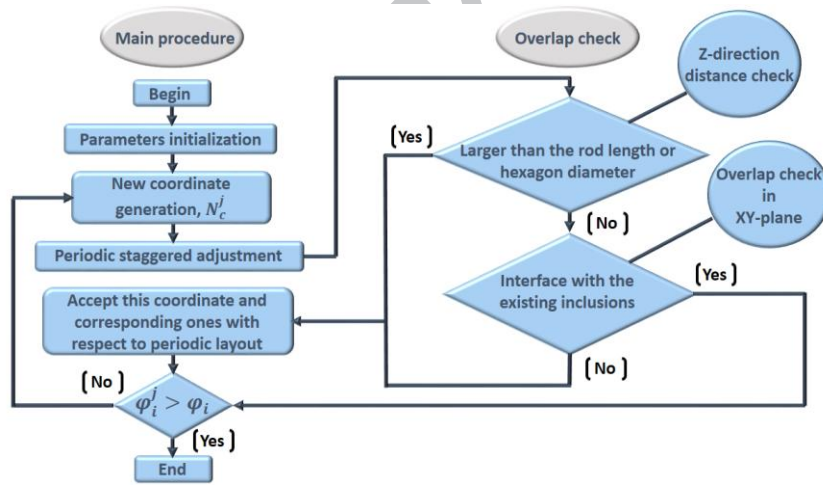

Fig.2. Flowchart of the 3D staggered hard-core algorithm (SHCA).

The SHCA includes a main procedure and an overlap check function. The main procedure begins with parameter initialization which consists of the RVE dimensions, inclusion shapes and aspect ratios, as well as, the desired inclusion volume fraction (φ_i). Subsequently, the new coordinate, $N_c^{\,j}$, for an inclusion is generated by a random function in the MATLAB code. Periodic

9

staggered adjustment is executed if the inclusion is adjacent to corners, exterior edges or surfaces of the RVE, then new coordinates will be generated to maintain geometric periodicity. Moreover, inclusion intersections for each generated coordinate are examined using the overlap check function. The depiction of overlap check functions for hexagonal and cylindrical inclusions are shown in Fig. 3 and Fig. 4 respectively. For the overlap check function for hexagonal inclusions, each hexagon edge and vertex must be checked to distinguish inclusion intersections. Fig. 3 (a) exhibits closest aggregate hexagons. Hexagon R_f in the middle is the reference one and the others are the nearest hexagons to R_f. In order to avoid inclusion intersections, the center of newly generated hexagon must be retained outside of the orange dash-dot line. Further depictions are indicated in the fourth quarter of the XY-plane in Fig. 3 (b) where O_r is the XY-coordinate origin and center of R_f, also, O_1, O_2, and O_3 are the center of three typical hexagons nearest to R_f. Thereupon, the function of the orange dash-line can be expressed as:

$$\begin{cases} |y' - y_r| = \sqrt{3}r, (\theta \geq 60°) \\ |y' - y_r| = \left(2\sqrt{3}r - \sqrt{3}\left(|x' - x_r|\right)\right), (\theta < 60°) \end{cases},$$

(10)

where (x_r, y_r) and (x', y') are the center coordinates of R_f and the newly generated hexagon respectively. r is the radius of the hexagon circumscribed circle, and θ is defined as:

$$\theta = \arctan\left(\left(y_r - y'\right)/\left(x_r - x'\right)\right)$$

(11)

The other three quadrants follow the same procedure to guarantee generation of newly non-intersected hexagons. With regards to inclusion intersections in the Z-direction, illustrated in Fig.

10

3 (c), the YZ-coordinates are checked if the Z-coordinate of the newly-generated hexagon is within range of R_f thickness.
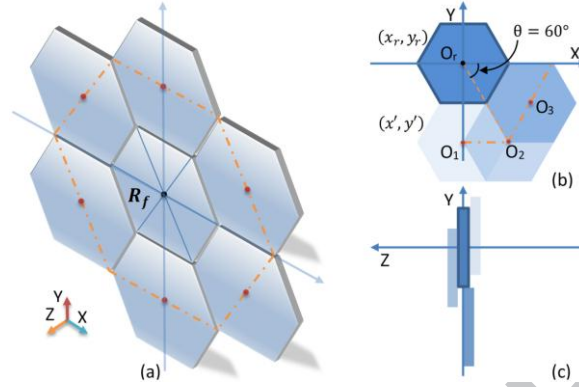

Fig.3. 3D and 2D views of overlap check function for hexagonal inclusions.

With regards to the overlap check function for cylindrical inclusions, analogous principals are applied. However, as is shown in Fig. 4 (a-b), in the XY-plane, the distance between cylinder R_f and newly generated cylinder must be greater than the R_f diameter while in Z-direction distance between two cylinders must be less than the cylinder length (see Fig. 4 (c)).
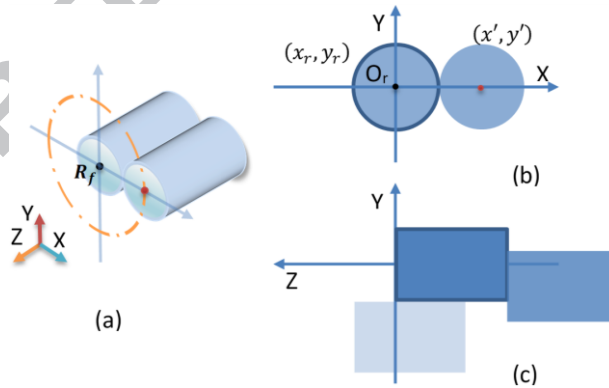

Fig.4. 3D and 2D views of overlap check function for cylindrical inclusions.

Finally, once the desired inclusion volume fraction is attained, the inclusion coordinates were imported into the commercial finite element software ABAQUS to produce 3D periodic

11

staggered and aligned RVEs using customized PYTHON scripts. Fig. 5 (a) and (b) depict the dimensions of both considered inclusions, along with the definition of aspect ratio, $\rho = L / h$.
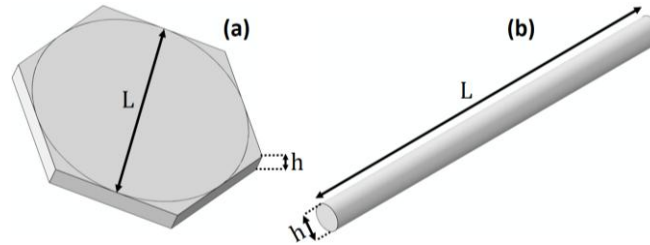

Fig.5. Inclusion dimensions used in aspect ratio (ρ) calculation for 3D RVE models. **(a)** hexagonal platelet inclusion, **(b)** cylindrical inclusion.

Three different aspect ratios (ρ = 5, 15, 25) for four inclusion volume fractions (φ_i = 10, 20, 30, 40) were explored for both hexagonal platelet and cylindrical inclusion RVE models. Due to the distinct shape of the inclusions considered, the corresponding 3D RVE sizes were different. The length, width, and height of the hexagonal platelet 3D RVE are 15, 15, and 5 μm. The length, width, and height of cylindrical inclusion 3D RVE are 5, 5, and 15 μm. Note that these chosen dimensions for 3D RVEs were based on a sensitivity analysis and are compared with experimental data in Section 4. Fig. 6 illustrates 3D RVEs generated with non-uniformly dispersed staggered hexagonal and aligned cylindrical inclusions for a 30% volume fraction, containing periodic geometries. Light blue particles are inclusions intersecting the outer surfaces providing periodic surface pairs, and yellow particles are inclusions within the RVE.
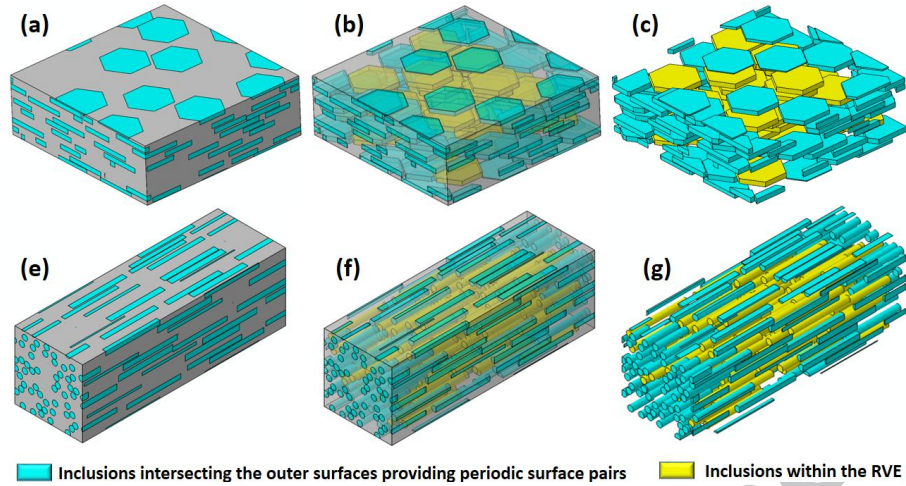
Fig.6. Generated periodic 3D RVEs with nonuniformly dispersed (a-c) staggered hexagonal and (e-g) aligned cylindrical inclusions with 30% volume fraction.

3.2. 3D assessment of inclusion spatial distribution in generated RVEs

The spatial distribution nonuniformity of the staggered and aligned inclusions within the generated RVEs was assessed using 3D spatial analysis functions, namely 3D autocorrelation analysis. In other studies, several 2D approaches have been used for this purpose including nearest neighbor analysis and Voronoi tessellation analysis [38-41]. 3D autocorrelation analysis describes the relative position of each inclusion in a region relative to not only the nearest inclusions but also, every other inclusion. Fig. 7 and Fig. 8 illustrate the 3D autocorrelation analyses for RVEs generated with non-uniformly staggered hexagonal and aligned cylindrical inclusions, respectively, both with inclusion volume fractions of 30%. The 3D autocorrelation diagram is depicted by taking one inclusion as the reference and plotting the relative positions of all other inclusions within a spherical space. This space is composed of several layers, and within each layer, the density of inclusions is utilized to define a density recovery profile (DRP) (see [40, 41] for more details). Fig. 7a and 8a show the 3D autocorrelation analysis DRPs for 3D RVEs with randomly dispersed inclusions. The remaining plots in Fig. 7b and 8b exhibit distance distributions and two direction distributions of the random inclusions relative to the reference

13

inclusion (i.e., azimuthal angle, theta, and elevation angle, phi), which make up the spherical coordinate autocorrelation tri-histogram plots. The constant DRP values at an average magnitude within the spherical space demonstrate that the generated 3D RVEs have consistent nonuniformly distributed inclusions. For the direction distribution analysis, the generated 3D RVEs have consistent inclusion densities in all radial directions for both the theta and phi angles, which is represented by circles with smooth edges. This further suggests that the inclusions within the generated 3D RVEs have consistent nonuniform random distributions, and thus accurately depict the microstructure of the studied materials.
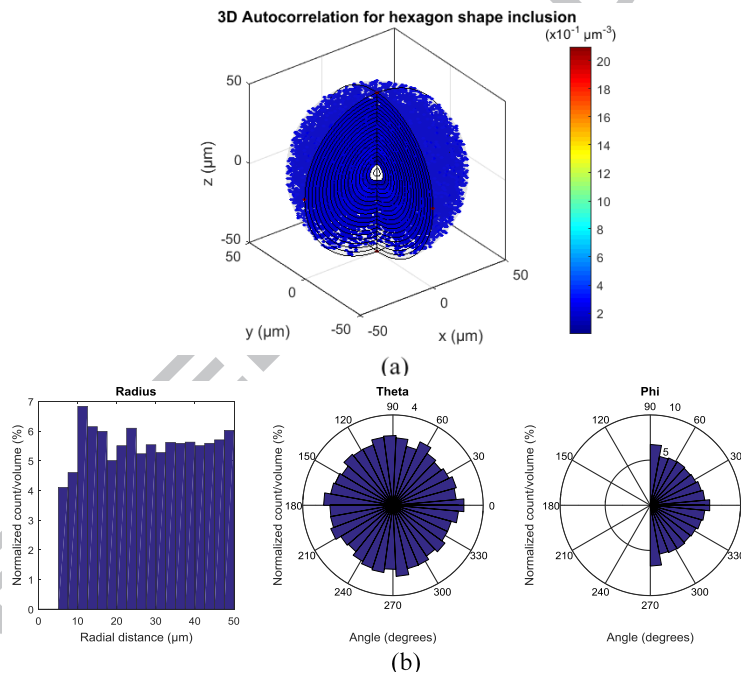

Fig.7. (**a**) 3D Autocorrelation analysis and density recovery profile (DRP) for 3D RVEs with hexagonal inclusions for 30% volume fraction. (**b**) autocorrelation tri-histogram plots.
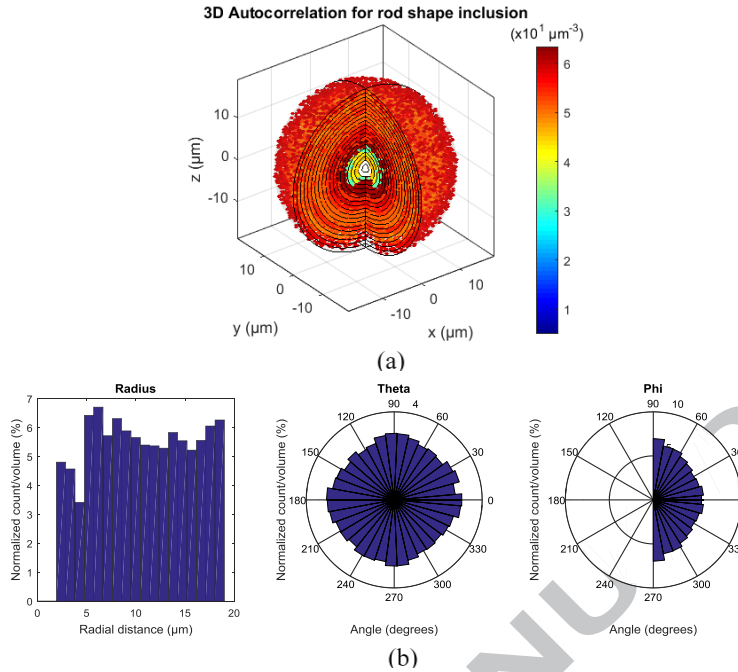
Fig.8. (a) 3D Autocorrelation analysis and density recovery profile (DRP) for 3D RVEs with cylindrical inclusions for 30% volume fraction. **(b)** autocorrelation tri-histogram plots.

The main benefits of the developed SCHA when compared to previously reported algorithms include (i) applicability for multiple distinct bio-inspired materials, (ii) rapid generation of 3D periodic staggered and aligned RVEs within minutes, and (iii) ability to generate 3D RVEs for high inclusion volume fractions (i.e., 40%). In practice, the developed algorithm can be employed to accurately evaluate homogenized material properties to be used in the macroscopic analysis of different bio-inspired composite structures.

3.3. Finite element modeling

The generated 3D RVEs, beginning with the creation of the RVE volumes, were subsequently implemented into ABAQUS using custom PYTHON algorithms for further preprocessing prior to analysis. In order to apply periodic boundary conditions (PBC) for the generated RVEs, a dummy element and copy mesh technique we previously developed in ABAQUS was employed in this study [37]. The technique is summarized in Fig.9. In the copy mesh method, only

15

tetrahedral elements with a diminutive seed size can be used. Hence, C3D4 elements with sizes less than $1/10^{th}$ of the cylindrical inclusion diameter and hexagonal platelet thickness were employed.
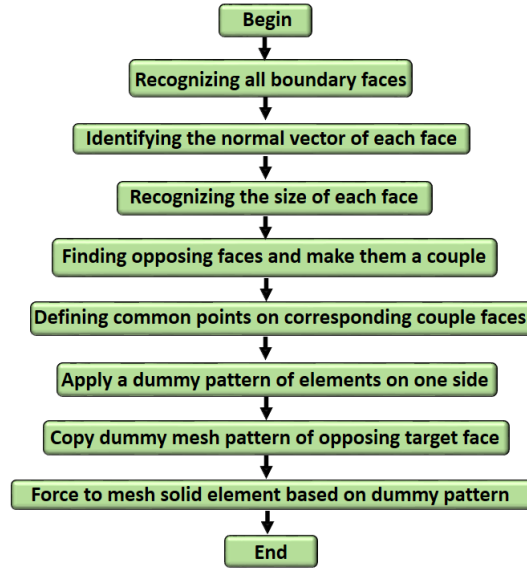

Fig.9. Flowchart of copy mesh module and dummy element technique for generating analogous mesh scheme on the opposing faces of periodic 3D RVEs.

PBCs were applied to the RVEs using translational symmetry derived by Li and co-workers [42, 43]. Based on Fig.10, the derivation of these boundary conditions can be defined as follows:

$$u_{Q'} - u_{T'} = u_Q - u_T$$

$$v_{Q'} - v_{T'} = v_Q - v_T \tag{12}$$

$$w_{Q'} - w_{T'} = w_Q - w_T$$

where u, v, and w are displacements in the x, y and z directions respectively. These equations can be rearranged as follows:

$$u_{Q'} - u_Q = u_{T'} - u_T$$

16

$$v_{Q'} - v_Q = v_{T'} - v_T \tag{13}$$
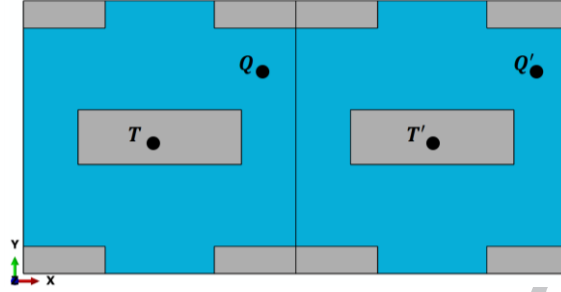
$$w_{Q'} - w_Q = w_{T'} - w_T$$

Fig.10. Periodic RVE where points Q' and T' are the image points of Q and T in the adjacent

RVE.

The relationship between six independent macroscopic strains (i.e., ε_x, ε_y, ε_z, ε_{yz}, ε_{xz}, ε_{xy}) can be

expressed as follows:

$$u' - u = (x' - x)\varepsilon_x + (y' - y)\varepsilon_{xy} + (z' - z)\varepsilon_{xz}$$

$$v' - v = (y' - y)\varepsilon_{xy} + (z' - z)\varepsilon_{yz} \tag{14}$$

$$w' - w = (z' - z)\varepsilon_z$$

where x', y', and z' are the coordinates of Q' or T' point. These equations can be written in

the form of translational symmetry transformations A, B, and C, where i, j and k represent the

number of RVE periods in x, y and z directions respectively.

$$(x' - x) = A(i, j, k) = 2ai$$

$$(y' - y) = B(i, j, k) = 2bj \tag{15}$$

17

$$(z'-z) = C(i,j,k) = 2ck$$

where 2*a*, 2b and 2c are the width, height and depth of the RVE respectively. By employing these equations and substituting values for i, j and k, periodic boundary conditions on the eight corners, twelve edges and six faces (see Fig.11) of the RVE can be applied. These relations are given in Table 2.
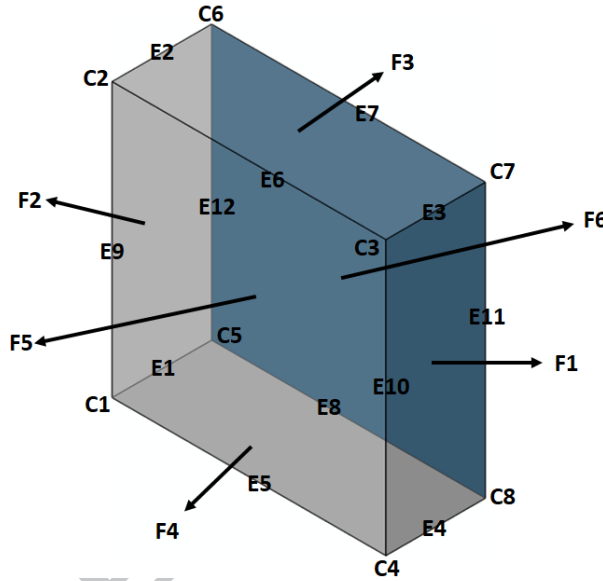
Fig.11. The labels of 3D RVE faces, edges, and corners for applying PBCs.

Table 2. PBCs equations for the faces, edges, and corners of 3D RVE.

Faces	Edges (E_1-E_4)	Edges (E_5-E_8)	Edges (E_9-E_{12})
$i=1, j=0, k=0$ $u_{F2}-u_{F1}=2a\varepsilon_x$ $v_{F2}-v_{F1}=0$ $w_{F2}-w_{F1}=0$	$i=0, j=1, k=0$ $u_{E2}-u_{E1}=2b\varepsilon_{xy}$ $v_{E2}-v_{E1}=2b\varepsilon_y$ $w_{E2}-w_{E1}=0$	$i=0, j=1, k=0$ $u_{E6}-u_{E5}=2b\varepsilon_{xy}$ $v_{E6}-v_{E5}=2b\varepsilon_y$ $w_{E6}-w_{E5}=0$	$i=1, j=0, k=0$ $u_{E10}-u_{E9}=2a\varepsilon_x$ $v_{E10}-v_{E9}=0$ $w_{E10}-w_{E9}=0$

18

$i=0, j=1, k=0$ $u_{F4} - u_{F3} = 2b\varepsilon_{xy}$ $v_{F4} - v_{F3} = 2b\varepsilon_y$ $w_{F4} - w_{F3} = 0$	$i=1, j=1, k=0$ $u_{E3} - u_{E1} = 2a\varepsilon_x + 2b\varepsilon_{xy}$ $v_{E3} - v_{E1} = 2b\varepsilon_y$ $w_{E3} - w_{E1} = 0$	$i=0, j=1, k=1$ $u_{E7} - u_{E5} = 2b\varepsilon_{xy} + 2c\varepsilon_{xz}$ $v_{E7} - v_{E5} = 2b\varepsilon_y + 2c\varepsilon_{yz}$ $w_{E7} - w_{E5} = 2c\varepsilon_z$	$i=1, j=0, k=1$ $u_{E11} - u_{E9} = 2a\varepsilon_x + 2c\varepsilon_{xz}$ $v_{E11} - v_{E9} = 2c\varepsilon_{yz}$ $w_{E11} - w_{E9} = 2c\varepsilon_z$
$i=0, j=0, k=1$ $u_{F6} - u_{F5} = 2c\varepsilon_{xz}$ $v_{F6} - v_{F5} = 2c\varepsilon_{yz}$ $w_{F6} - w_{F5} = 2c\varepsilon_z$	$i=1, j=0, k=0$ $u_{E4} - u_{E1} = 2a\varepsilon_x$ $v_{E4} - v_{E1} = 0$ $w_{E4} - w_{E1} = 0$	$i=0, j=0, k=1$ $u_{E8} - u_{E5} = 2c\varepsilon_{xz}$ $v_{E8} - v_{E5} = 2c\varepsilon_{yz}$ $w_{E8} - w_{E5} = 2c\varepsilon_z$	$i=0, j=0, k=1$ $u_{E12} - u_{E9} = 2c\varepsilon_{xz}$ $v_{E12} - v_{E9} = 2c\varepsilon_{yz}$ $w_{E12} - w_{E9} = 2c\varepsilon_z$

Corners

$i=0, j=1, k=0$ $u_{C2} - u_{C1} = 2b\varepsilon_{xy}$ $v_{C2} - v_{C1} = 2b\varepsilon_y$ $w_{C2} - w_{C1} = 0$	$i=1, j=1, k=0$ $u_{C3} - u_{C1} = 2a\varepsilon_x + 2b\varepsilon_{xy}$ $v_{C3} - v_{C1} = 2b\varepsilon_y$ $w_{C3} - w_{C1} = 0$	$i=1, j=0, k=0$ $u_{C4} - u_{C1} = 2a\varepsilon_{xz}$ $v_{C4} - v_{C1} = 0$ $w_{C4} - w_{C1} = 0$	$i=0, j=0, k=1$ $u_{C5} - u_{C1} = 2c\varepsilon_{xz}$ $v_{C5} - v_{C1} = 2c\varepsilon_{yz}$ $w_{C5} - w_{C1} = 2c\varepsilon_z$
$i=0, j=1, k=1$ $u_{C6} - u_{C1} = 2b\varepsilon_{xy} + 2c\varepsilon_{xz}$ $v_{C6} - v_{C1} = 2b\varepsilon_y + 2c\varepsilon_{yz}$ $w_{C6} - w_{C1} = 2c\varepsilon_z$	$i=0, j=0, k=1$ $u_{C7} - u_{C1} = 2a\varepsilon_x + 2b\varepsilon_{xy} + 2c\varepsilon_{xz}$ $v_{C7} - v_{C1} = 2b\varepsilon_y + 2c\varepsilon_{yz}$ $w_{C7} - w_{C1} = 2c\varepsilon_z$	$i=0, j=0, k=1$ $u_{C8} - u_{C1} = 2a\varepsilon_x + 2c\varepsilon_{xz}$ $v_{C8} - v_{C1} = 2c\varepsilon_{yz}$ $w_{C8} - w_{C1} = 2c\varepsilon_z$	

Isotropic linear elastic properties were designated for both inclusions and matrix. Their interface was modeled as perfectly bonded; given that this is a study of the elastic behavior, this approach is suitable. The Young's modulus and Poisson's ratio of the inclusions and matrix were assigned

as E_i =330 GPa, $\nu_i = 0.2$, E_m =1.88 GPa, and $\nu_m = 0.4$ for all generated RVEs, which are typical values for stiff alumina inclusions and chitosan polymer, respectively, and allowed for a comparison with results reported in Ref. [11]. For additional comparisons between the predicted results and reported experimental data for the cylindrical inclusion RVE model, constituent properties were taken from Ref. [44].

For the purpose of computing the bulk mechanical properties of the bio-inspired composite materials using the generated 3D RVEs, a homogenization process shown in Fig. 12 was employed [37, 45, 46]. Fig. 12(a) illustrates a heterogeneous periodic microstructure with volume, φ, under external forces per area, $\bar{F}$, on the boundaries, A_t, as well as exterior displacements per area, $\bar{u}$, on boundaries, A_u. Equilibrium relations, strain-displacement law, constitutive equations, and boundary conditions for a heterogeneous microstructure can be expressed using Eq. (16) to Eq. (20) respectively.

$$\sigma_{ij,j} + f_i = 0 \text{ in } \varphi, \tag{16}$$

$$\varepsilon_{ij} = \frac{1}{2}(u_{i,j} + u_{j,i}) \text{ in } \varphi, \tag{17}$$

$$\sigma_{ij} = C_{ijkl}\varepsilon_{kl} \text{ in } \varphi, \tag{18}$$

$$\sigma_{ij}n_j = \bar{F}_i \text{ on } A_t, \tag{19}$$

$$u_i = \bar{u}_i \text{ on } A_u, \tag{20}$$

where $\sigma_{ij,j}$ are the derivatives of stress components with respect to j, f_i are the prescribed body forces per unit volume, ε_{ij} represents strain components in equilibrium equations, C_{ijkl} is

20

the linear elastic material stiffness matrix, n_j denotes outward normal vectors on the volume boundaries. For inhomogeneous materials such as nacre-like composites, the stiffness matrix may vary in different regions of the microstructure, and hence the solution of Eqs. (16-20) becomes intricate. Therefore, addressing homogenized responses or averaged mechanical properties is essential for continuum-based calculations. As indicated in Fig. 11 (b), by means of a simple RVE or unit cell with volume, φ_e, a heterogeneous periodic microstructure can be generated for homogenization. The terms φ_m and φ_i denote the matrix and inclusions volume fraction of the RVE respectively. Thus, $\varphi_e = \varphi_m \bigcup \varphi_i$ is the total volume of the RVE, and $A_e = A_{tm} \bigcup A_{um}$ represents the summation of exterior boundaries, where A_{tm} and A_{um} are regions under tractions and displacements respectively.
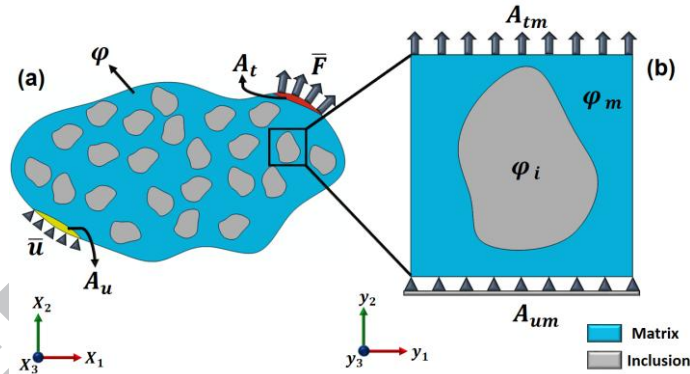

Fig.12. **(a)** Heterogeneous periodic microstructure of a representative biomimetic composite **(b)** a representative volume element (RVE) of composite microstructure with inclusion and matrix phases.

Jansson [45] derived the relation between volume average stress and volume average strain for the inhomogeneous materials which were defined as:

$$\left\langle \varepsilon_{ij} \right\rangle = \frac{1}{\left| \varphi_e \right|} \int_\varphi \varepsilon_{ij}^0 (x, y) d\varphi_e = \varepsilon_{ij}^{(0)} \tag{21}$$

$$\left\langle \sigma_{ij} \right\rangle = \frac{1}{\left| \varphi_e \right|} \int_\Psi \sigma_{ij}^0 (x,y) d\varphi_e = C_{ijkl}^H (\varepsilon^0) \left\langle \varepsilon_{kl} \right\rangle, \tag{22}$$

where $\left\langle \varepsilon_{ij} \right\rangle$ and $\left\langle \sigma_{ij} \right\rangle$ are sequentially volume averaged strain and stress for the RVE. ε_{ij}^0 and σ_{ij}^0 denote local strain and stress in the RVE respectively. The equivalent homogenized stiffness matrix is introduced by C_{ijkl}^H. For a homogenized elastic microstructure, the relation between stress and strain can be expressed via Eq.(23). Additionally, for 3D RVEs, C_{ijkl}^H constants are calculated via applying six independent unit macrostrains and PBCs for six independent models. $\varepsilon_{ij}^{(0)} = \frac{1}{2} (\frac{\partial u_i^0}{\partial x_j} + \frac{\partial u_j^0}{\partial x_i})$ expresses imposed unit macroscopic strains for any mentioned six independent loading cases. Thus, by means of the computed volume averaged stresses and strains in each case, one column of effective stiffness matrix can be calculated using the following:

$$\begin{bmatrix} \sigma_{11} \\ \sigma_{22} \\ \sigma_{33} \\ \tau_{23} \\ \tau_{13} \\ \tau_{12} \end{bmatrix} = \begin{bmatrix} C_{11} & C_{12} & C_{13} & 0 & 0 & 0 \\ C_{12} & C_{22} & C_{23} & 0 & 0 & 0 \\ C_{13} & C_{23} & C_{33} & 0 & 0 & 0 \\ 0 & 0 & 0 & C_{44} & 0 & 0 \\ 0 & 0 & 0 & 0 & C_{55} & 0 \\ 0 & 0 & 0 & 0 & 0 & C_{66} \end{bmatrix} \begin{bmatrix} \varepsilon_{11} \\ \varepsilon_{22} \\ \varepsilon_{33} \\ \gamma_{23} \\ \gamma_{13} \\ \gamma_{12} \end{bmatrix} \tag{23}$$

The inverted form of C_{ijkl}^H matrix is compliance matrix S_{ijkl}^H. The elastic constants are calculated using the following S_{ijkl}^H coefficients:

$$[C]=[S]^{-1}\rightarrow[S]=\begin{bmatrix} \dfrac{1}{E_1} & \dfrac{-v_{21}}{E_2} & \dfrac{-v_{31}}{E_3} & 0 & 0 & 0 \\[2mm] \dfrac{-v_{21}}{E_2} & \dfrac{1}{E_2} & \dfrac{-v_{32}}{E_3} & 0 & 0 & 0 \\[2mm] \dfrac{-v_{31}}{E_3} & \dfrac{-v_{32}}{E_3} & \dfrac{1}{E_3} & 0 & 0 & 0 \\[2mm] 0 & 0 & 0 & \dfrac{1}{G_{23}} & 0 & 0 \\[2mm] 0 & 0 & 0 & 0 & \dfrac{1}{G_{13}} & 0 \\[2mm] 0 & 0 & 0 & 0 & 0 & \dfrac{1}{G_{12}} \end{bmatrix} \tag{24}$$

In this study, the volume averaged stresses and strains, i.e., Eqs. (21-22), were computed numerically for all RVEs, and the elastic constants were calculated using Eqs. (23-24). The results are presented in Section 4.

4. Results and discussion

The numerical results computed using the developed 3D RVE FE models and constituent properties outlined in Section 3 are presented subsequently. First, normalized volume averaged elastic moduli, E/E_m calculated using homogenization theory are compared with predictions using the analytical models presented in section 2, as well as experimental data from the literature for two different material systems. Then, the capabilities of assessing in- and out-of-plane orthotropic elastic properties for the developed 3D RVEs are also presented.

4.1. Comparison with experimental data, analytical models, and 2D RVEs

In order to highlight the deformation of the generated 3D RVEs and accurate use of periodic boundary conditions for both normal and shear loading conditions, typical normal and shear stress contours for RVEs with $\varphi_i = 30\%$ and $\rho = 15$ are shown in Fig. 13 (a-b) and Fig. 14 (a-b). The applied strain for all normal and pure shear loading cases was 0.5%. The stress contours reveal the variability of stress at the inclusion/matrix interfaces within the 3D RVE resulting

23

from the staggered non-uniform inclusion dispersion. Furthermore, the characteristic shear lag behavior for both models under an applied normal strain can be observed via the shear stress contours in the matrix (see Fig. 13 (a) and 14 (a)). In this case, the shear lag response is not as pronounced as one would observe for lower volume fractions due to the influence of surrounding inclusions and their constraining effect on the matrix, which highlights the importance of considering the inclusion geometry and non-uniform inclusion dispersion in a prediction model. Similarly, as expected the peak normal stress in the fibers of the cylindrical RVE model under an applied normal strain occurs at the fiber center and reduces towards the fiber ends. The variability in stress magnitudes between adjacent fibers is also a result of the constraining effect between the fibers and their nonuniform dispersion.
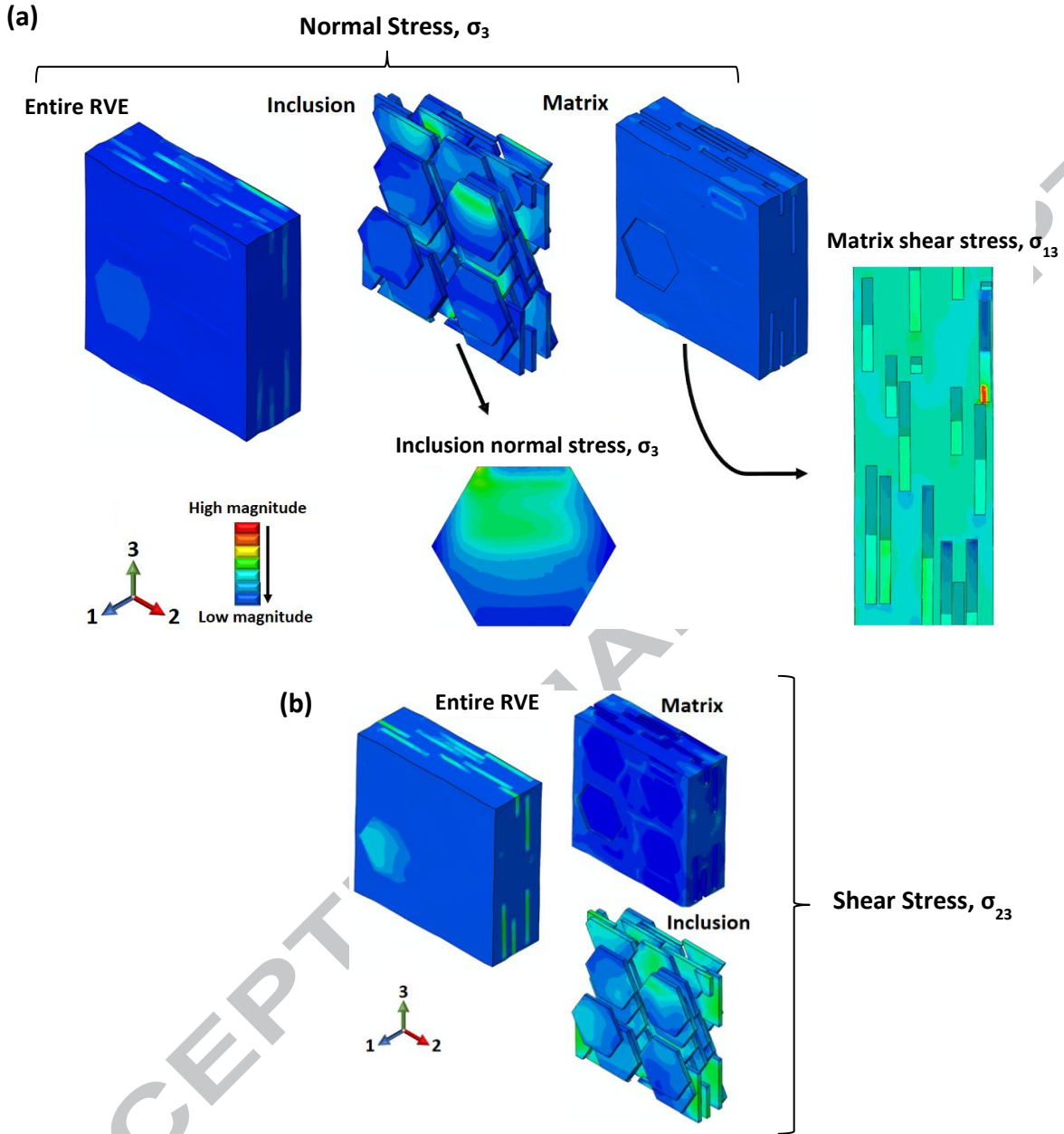
Fig.13. Stress contours for hexagonal inclusion RVE model with **(a)** uniaxial applied load along 3-direction, **(b)** pure shear applied in 23-plane.
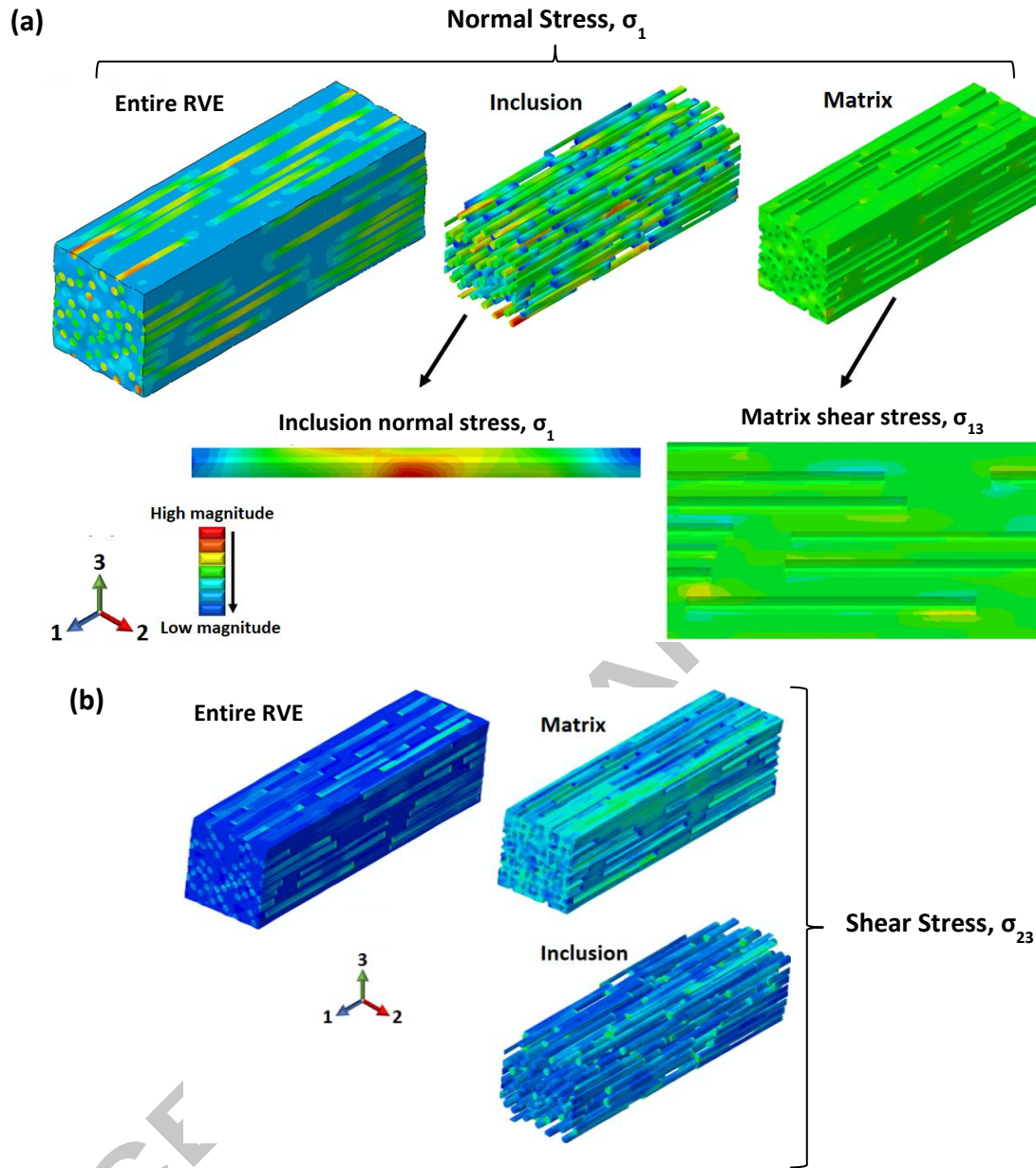
Fig.14. Stress contours for cylindrical inclusion RVE model with **(a)** uniaxial applied load along 1-direction, **(b)** pure shear applied in 23-plane.

Table 2 indicates a comparison among computed normalized moduli E_2/E_m values for five hexagonal platelet models with randomly generated non-uniform particle dispersion morphologies, along with results from the analytical models presented in section 2, as well as, experimental data of a nacre-mimetic material generated using alumina micro-platelets and

chitosan by Mirkhalaf and Barthelat [11]. All have 10% inclusion volume fraction. Similarly, Table 3 presents another comparison among calculated normalized modulus, E_1/E_m, values for five cylindrical inclusion models with randomly generated non-uniform particle distribution morphologies, along with results from the presented analytical models in section 2, and experimental data for a short carbon fiber/polypropylene composite having 10% fiber volume fraction studied by Fu et al. [44]. It should be noted that the constituent material properties and inclusion aspect ratios used here for the cylindrical inclusion RVE models were taken from Ref. [44]. As it is evident from Tables 2 and 3, the average deviation of 3D RVE results with experimental data is approximately 5% for both models and each morphology, demonstrating an excellent agreement. The minor deviations may be due to assuming perfectly aligned inclusions in the 3D RVE models, while the real material could have several inclusion misalignments. Note that a number of 3D RVEs with different dimensions were considered to determine a suitable size. Based on the very good agreement with experimental data in Table 2 and 3, the selected volume for the hexagonal and cylindrical inclusion models were 1125 and 375 μm^3, and used for all subsequent predictions.

The higher deviation of analytical models from both experimental and 3D RVE results can be seen for both material systems. However, among these analytical models, the modified shear lag model has a good agreement for hexagonal platelet inclusion (Table 2) with both experimental and 3D RVE results. Other studies also used different versions of the shear lag model to predict the mechanical responses of platelet inclusion bio-inspired composites [8-10]. Regarding cylindrical inclusions, Mori-Tanaka model has a good agreement with both experimental and 3D RVE results compared to other analytical models (Table 3). More details of reasons for these deviations will be discussed in the following paragraph.

Table.2 Comparison between normalized moduli (E_2/E_m) from 3D RVEs (5 trials), analytical models, and experimental data of a nacre-mimetic material (i.e., alumina/chitosan) with a volume fraction (φ_i) of 10%. Error is calculated against the experimental data.

	3D RVE Trial 1	3D RVE Trial 2	3D RVE Trial 3	3D RVE Trial 4	3D RVE Trial 5	3D RVE Avg.	Mori-Tanaka	Mod. shear-lag	H-T	Exp [11]
E_2/E_m	3.72	3.75	3.70	3.69	3.73	3.72	3.30	3.76	3.88	3.56
Error (%)	4.61	5.48	3.96	3.65	4.95	4.53	7.37	5.78	8.98	-

Table.3 Comparison between normalized moduli (E_1/E_m) from 3D RVEs (5 trials), analytical models and experimental data from a short carbon fiber/polypropylene composite having a volume fraction (φ_i) of 10%.

	3D RVE Trial 1	3D RVE Trial 2	3D RVE Trial 3	3D RVE Trial 4	3D RVE Trial 5	3D RVE Avg.	Mori-Tanaka	Mod. shear-lag	H-T	Exp [44]
E_1/E_m	9.11	8.92	9.00	9.01	9.15	9.04	9.33	9.41	6.82	8.58
Error (%)	6.08	3.92	4.85	4.95	6.63	5.28	8.66	9.60	20.54	-

Figures 15 (a-b) compare the predictions for E_2 from hexagonal inclusion 3D RVE model and E_1 for cylindrical inclusion 3D RVE model with the aforementioned analytical models. For the Mori-Tanaka model, the inclusion shape was approximated as ellipsoidal with a perfectly aligned distribution assumption. As seen in these figures, for lower aspect ratios, the analytical model predictions are close to those of the 3D RVEs for both inclusion shapes. However, with increasing volume fraction and aspect ratio, the discrepancy between 3D RVE and analytical models tends to increase. According to previous studies [39], inaccurate predictions for higher aspect ratios and volume fractions for shear lag and Halpin-Tsai models are expected since they

28

do not accurately account for the inclusion shape, their dispersions and three-dimensional effects, including inclusion overlap, which are characteristic of realistic microstructures. Modified shear lag models [8-10], which are often used for bio-inspired composites, have similar limitations and thus cannot be used to predict all elastic constants. The reason for notable discrepancies between the Mori-Tanaka model and the 3D RVEs, particularly for higher volume fractions, stems from assuming ellipsoidal shape inclusions instead of cylindrical and hexagonal shapes as well as assuming non-realistic inclusion dispersions. Previous studies have reported inaccuracies with the Mori-Tanaka model for higher aspect ratios [22, 47, 48]. By accurately representing inclusion shape/size and their realistic non-uniform dispersion in three dimensions, such as with the 3D RVE models reported herein, the local stress field variability and cylindrical inclusion interactions can be considered, which allows for prediction of all orthotropic elastic constants.
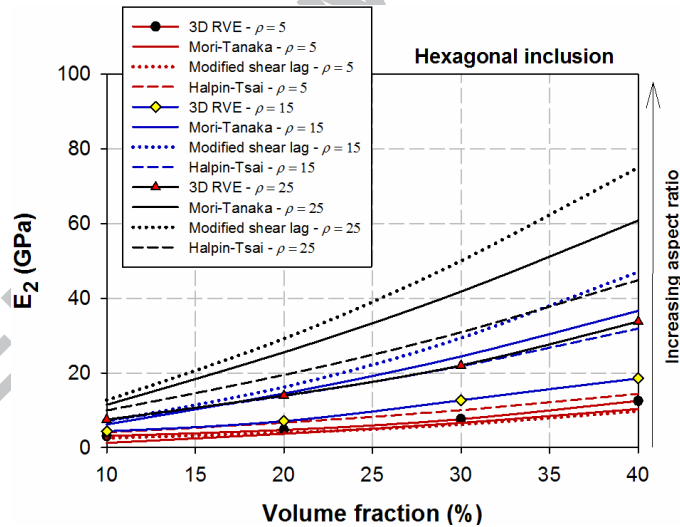
(a)
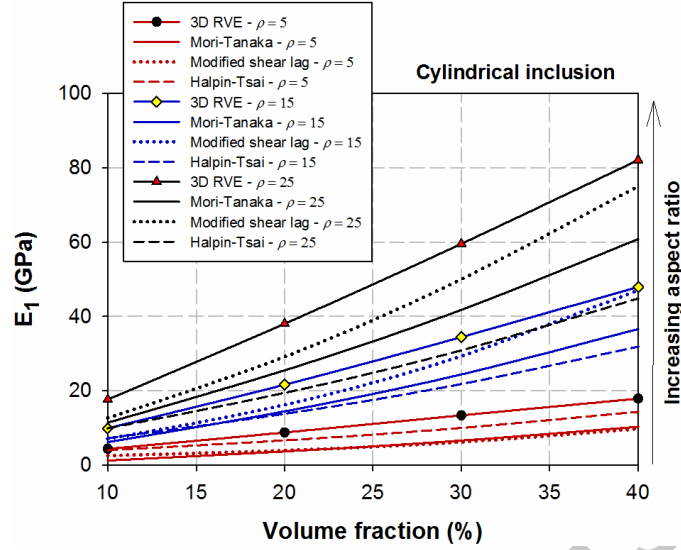
(b)

Fig.15. Comparisons of Young's modulus versus volume fraction for different aspect ratios among established analytical models (i.e., Mori-Tanaka, modified shear lag, and Halpin-Tsai) and 3D RVE results **(a)** E_2 for hexagonal platelet and **(b)** E_1 for cylindrical inclusions model.

Figures 16 (a-b) demonstrate further comparisons between the results predicted with the 3D RVE model and that of the Mori-Tanaka method, particularly the in-plane shear modulus G_{12} and Poisson's ratio ν_{12}. As seen in these figures, although the results for very low inclusion volume fractions are comparable, there are large discrepancies between the Mori-Tanaka model and the 3D RVE model predictions with increasing inclusion volume fractions. According to previous studies [22], inaccurate predictions for shear modulus for the Mori-Tanaka model are expected.
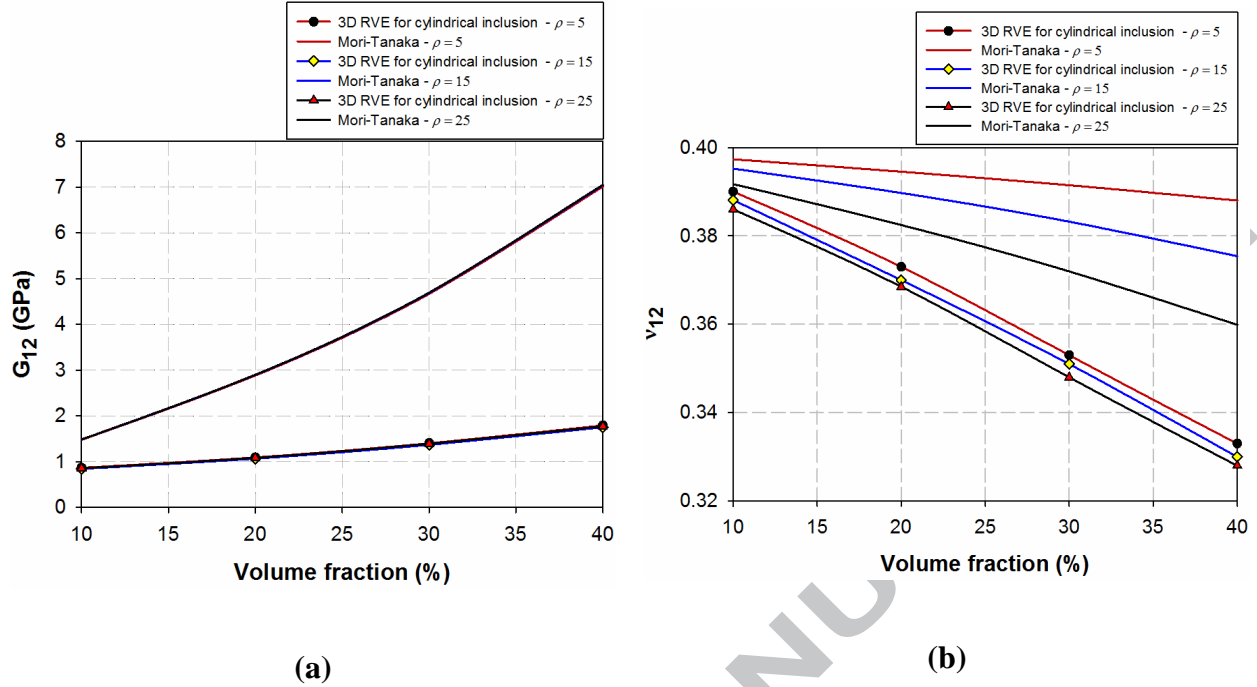
(a)

(b)

Fig.16. Comparisons of in-plane **(a)** shear modulus and **(b)** Poisson's ratio versus volume fraction for cylindrical inclusion 3D RVEs and the Mori-Tanaka analytical model for different aspect ratios.

The importance of accurately considering the shape, size and three-dimensional non-uniform dispersion of inclusions in bio-inspired composites is highlighted through the results presented in this paper. Here, the need to consider a 3D analysis versus a 2D 'plane strain' analysis, which is often assumed in many analytical and computational models of bio-inspired composites, will be discussed. Figure 17 shows the predicted variation of normalized Young's modulus with inclusion volume fraction along the fiber direction (E_1) for a composite with aligned cylindrical inclusions and along the in-plane direction (E_2) for a composite with hexagonal platelet inclusions. The results from a 2D RVE model reported by Mirkhalaf and Barthelat [11], where the hexagonal inclusion shape is simplified as a rectangle, is also included in Fig. 12. Note that the constituent properties (i.e., E_i =330 GPa, $v_i = 0.2$, E_m =1.88 GPa, and $v_m = 0.4$) and inclusion aspect ratio (i.e., ρ = 15) for all three of the models are the same. Although the

31

predicted results for the hexagonal platelet 3D RVE model are comparable with the 2D RVE model predictions, there is a notable discrepancy with the results from the cylindrical inclusion 3D RVE. The reason for this discrepancy stems from the inclusion cross-sectional shape and the corresponding inclusion dispersion. Based on the tri-histogram plots in Fig. 7 and 8, the variations of theta and phi for   cylindrical inclusions are lower than hexagonal platelet. This implies that cylindrical inclusions can achieve better packing than hexagonal (rectangular cross-section) inclusions [20]. This increases the efficiency of the load transfer from the matrix to the inclusions, thus leading to a stiffer RVE relative to the hexagonal platelet RVE at the same volume fraction [22]. Therefore, a 2D RVE model under predicts the stiffness of cylindrical inclusion bio-inspired composites in the fiber direction. Furthermore, 2D RVEs cannot provide all the orthotropic elastic constants, whereas 3D RVEs can.
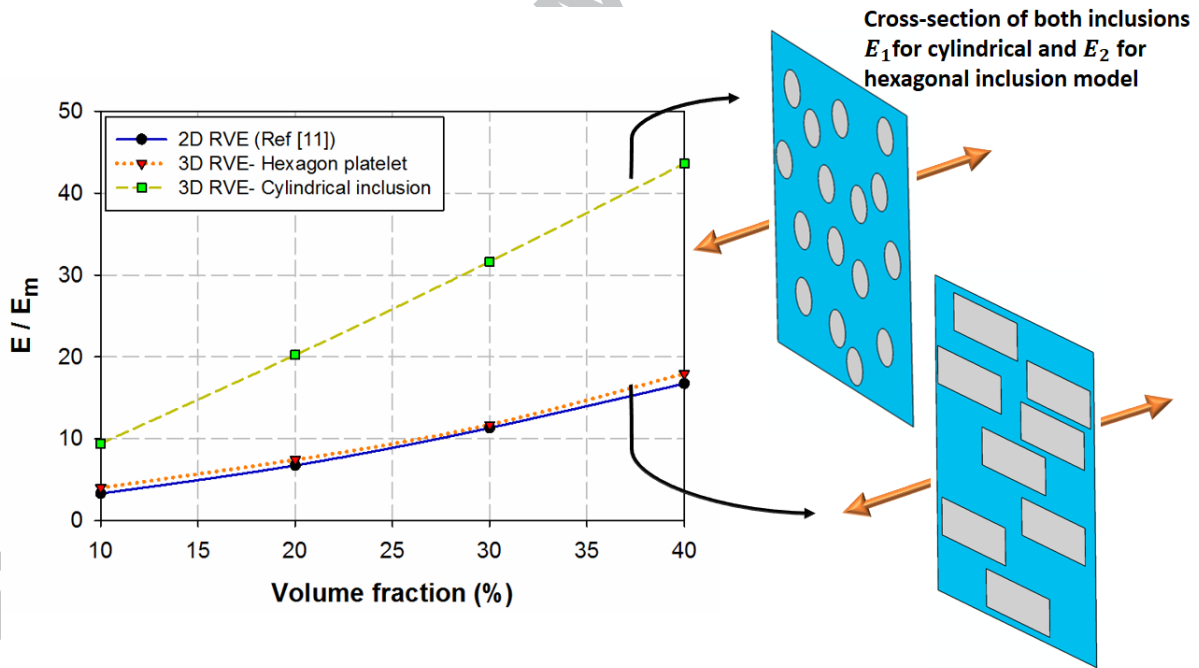

Fig.17. Comparison of normalized Young's modulus (E / E_m, where E_m is the Young's modulus of the matrix) versus volume fraction between 2D RVE and both 3D RVE models (i.e., hexagon platelet in-plane (E_2 or E_3) and cylindrical inclusion in the longitudinal direction (E_1)).

32

4.2. Prediction of orthotropic elastic constants

To demonstrate the capabilities of the developed 3D RVE models for predicting all in- and out-of-plane elastic constants, a series of simulations were performed using the constituent properties outlined in Section 3. Figures 18 (a-e) illustrate the predicted elastic constants versus volume fraction (φ_i) with various aspect ratios ($\rho = 5, 15, 25$) for the hexagonal platelet 3D RVE model. Note that all directions and planes for this model were defined based on the coordinate system indicated in Fig. 9. Fig. 18 (a) demonstrates the non-linear relationship between E_2 and φ_i and between E_3 and φ_i. By increasing φ_i from 10% to 40%, the discrepancy between each aspect ratio (ρ) tends to be increased. For the hexagonal platelet model, a direct relationship exists between L and E_2 or E_3 based on isostrain equations; thus, by enlarging L for a constant volume fraction, E_2 and E_3 should increase. Transverse isotropic properties can be implied by the approximately identical values of E_2 and E_3 for a given volume fraction, which is expected since the platelet inclusions are staggered and non-uniformly dispersed. Fig. 18 (b) shows the expected linear relationship of E_1 with volume fraction for all aspect ratios (ρ). According to micromechanical analytical models, such as the Rule of Mixtures, in a variety of composites, E_1 has a direct and linear relation with volume fraction [22]. In addition, in the platelet model, by increasing volume fraction or aspect ratio, cross-sectional overlaps among platelets are created; therefore, E_1 increased linearly. The approximately linear relationship between G_{12} and volume fraction (φ_i) and between G_{13} and volume fraction (φ_i) are shown in Fig. 18 (c). By increasing ρ, the nonlinear trend of these out-of-plane shear moduli, tend to increase through φ_i. The nonlinear trend of in-plane shear modulus G_{23} versus φ_i is represented in Fig. 18 (d). The discrepancy between each ρ tends to increase with φ_i due to the complex shape of the

hexagonal inclusions. Also, by increasing L and the area of hexagons, the effect of increased cross-sectional overlaps among platelets in shear modulus can be seen in this figure. Furthermore, the nonlinear relationship of ν_{12}, ν_{13}, and ν_{23} which are in- and out-of-plane Poisson's ratios versus φ_i are presented via Fig. 18 (e). The similarity between ν_{12} and ν_{13} for different volume fractions and aspect ratios further confirms that the predicted properties are consistent with a transversely isotropic material. It is evident in this figure that the nonlinearity of in-plane Poisson's ratio (ν_{23}) versus φ_i is slightly greater than out-of-plane Poisson's ratios, which may be attributed to the hexagonal shape of the particles. It can be noted that the size of micro-platelets (i.e., aspect ratio (ρ)) in these types of microstructures can play a pivotal role in mechanical performances for various bio-inspired material systems and applications [8-10].
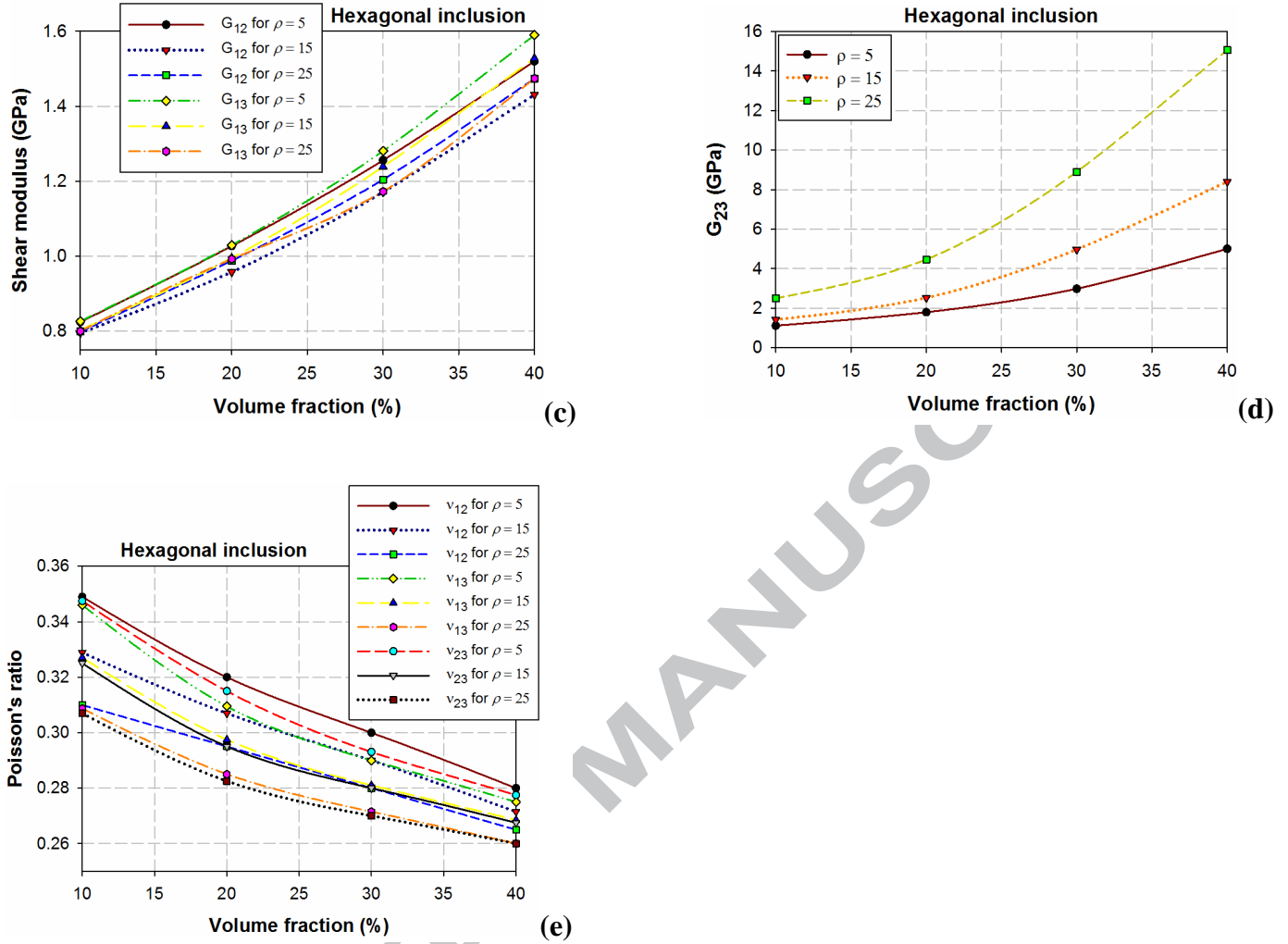

(a)

(b)

(c)

(d)

(e)
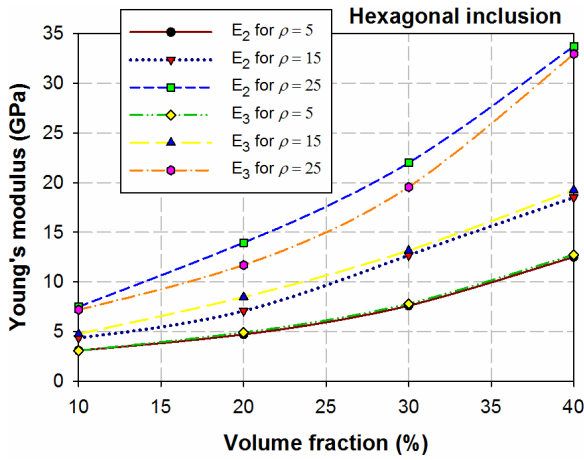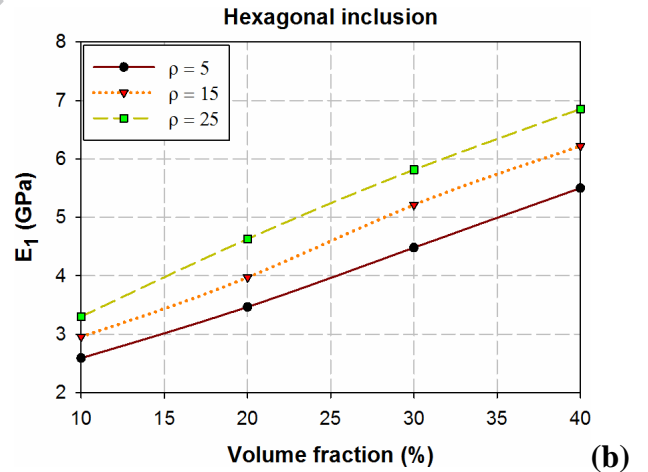
Fig.18. Predicted orthotropic elastic constants for hexagonal platelet model versus volume fraction (φ_i) for various aspect ratios. **(a)** E_2, E_3, **(b)** E_1, **(c)** G_{12}, G_{13}, **(d)** G_{23}, and **(g)** ν_{12}, ν_{13}, and ν_{23}.

Similar results for the cylindrical inclusion 3D RVE model are presented in Fig. 19 (a-e). Directions and planes for this model were defined with the coordinate system in Fig. 10. The similar non-linear relationship between E_2 and E_3 versus φ_i is shown by Fig. 19 (a). Unlike the hexagonal platelet model, by increasing φ_i from 10% to 40%, the discrepancies between aspect ratios (ρ) are relatively minor. The reason for these differences are likely due to the shape of the inclusion. By increasing the length of the cylinders (L), the inclusion enlarges only in the

35

longitudinal direction. Therefore, the transverse moduli, E_2 and E_3, are not greatly affected. However, by increasing L in the hexagon platelet model, the particle is enlarged in both transverse directions. This affects E_2 and E_3. Similar to the hexagonal platelet model, this model also demonstrates transverse isotropy, as one would expect due to the aligned cylindrical inclusions. The linear behavior of E_1 is displayed via Fig. 19 (b), which is consistent with other aligned discontinuous cylindrical inclusion composites [22, 49]. For the cylindrical inclusion model, the relationship of G_{12}, G_{13}, and G_{23} with volume fraction shown in Fig. 19 (c) demonstrates greater nonlinearity when compared to the hexagonal platelet model. The reason for this greater nonlinearity may be that for higher volume fractions, the degree of non-uniformity of the cylindrical inclusion tends to be greater when compared with the platelets. Therefore, the discontinuity of cross-sectional overlaps among cylindrical inclusion tends to be decreased leading to the higher magnitudes for G_{12}, G_{13}, and G_{23}. However, discrepancies among different aspect ratios (ρ) are negligible for shear modulus due to the shape of cylinder. Due to a direct relation between Poisson's ratio and the volume fraction of stiff inclusions, Fig. 19 (d) shows a linear behavior of ν_{12} and ν_{13} which gradually decrease with increasing volume fraction (φ_i). Also, because of the transverse isotropic nature of this model, the trend of ν_{12} and ν_{13} is approximately identical. The decreasing nonlinear behavior of ν_{23} versus φ_i is represented in Fig. 19 (e). ν_{23} is greater in magnitude compared to the in-plane Poisson's ratios, and this is consistent with other aligned fiber-reinforced composites [22, 49]. The results presented in Figs. 18 and 19 demonstrate that unlike the hexagonal platelet model, in the cylindrical inclusion model, elastic coefficients were not sensitive to aspect ratios (ρ), except for E_1 and ν_{23}. Understanding this issue can be effective in passing several obstacles in generating and applying bio-inspired composites.
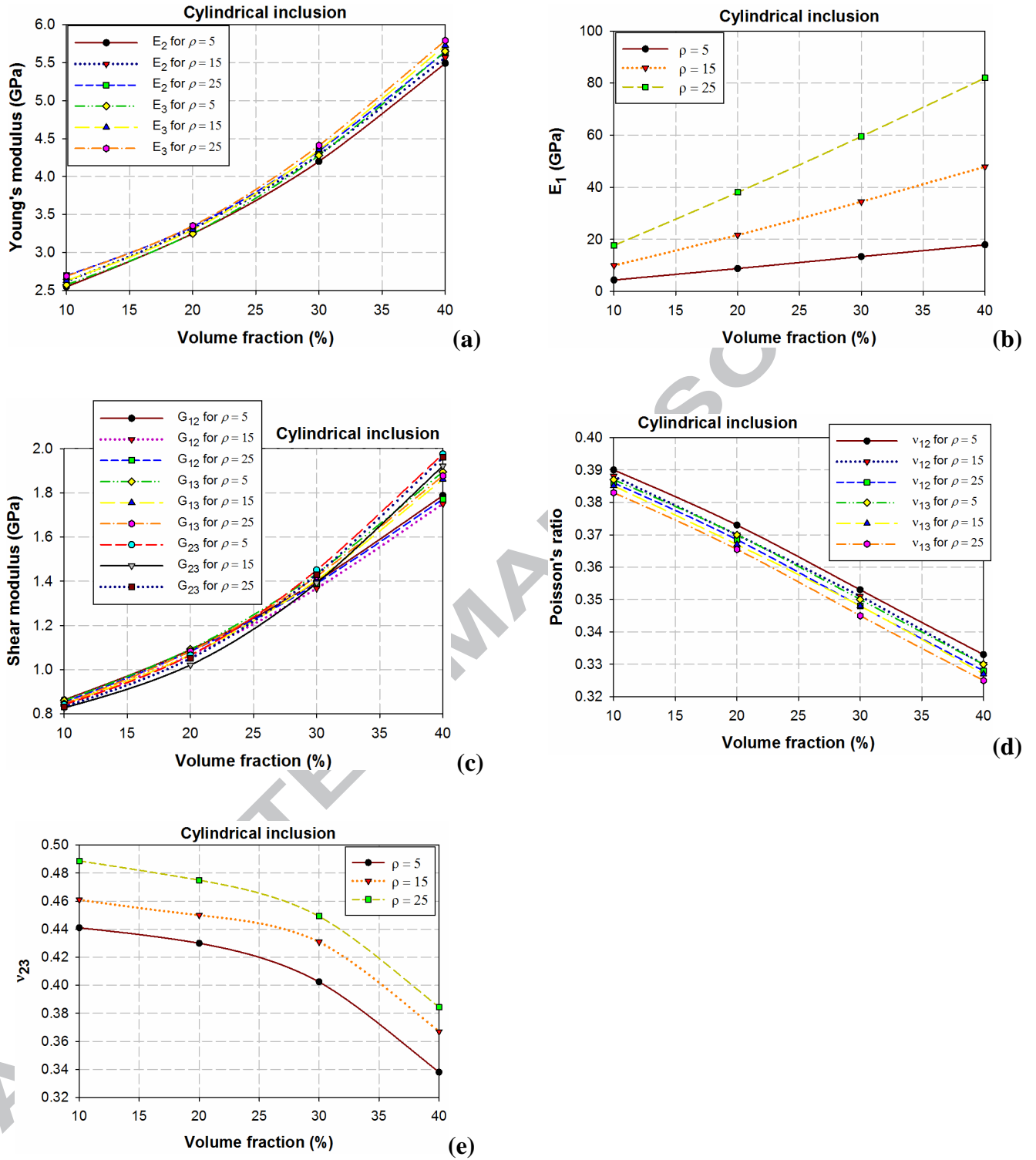
Fig.19. Predicted orthotropic elastic constants for cylindrical inclusion model versus volume fraction (φ_i) for various aspect ratios **(a)** E_2, E_3, **(b)** E_1, **(c)** G_{12}, G_{13}, G_{23}, **(d)** v_{12}, v_{13}, and **(e)** v_{23}.

4.3. General discussion

The presented results for two different bio-inspired composites have demonstrated that 3D RVEs with realistic non-uniform staggered inclusion dispersions that account for appropriate inclusion size and geometry, are critical for assessing their mechanical behavior. In fact, the local constraining effects for higher volume fractions can only be captured with such a model. Thus, the effect of the third dimension and the ability to simulate the actual response of inclusion-reinforced bio-inspired composites in all directions is a significant advancement. Employing the SHCA for generating non-uniformly staggered and aligned 3D RVEs of two different bio-inspired composites can be an effective method due to its straightforward and rapid nature. Consequently, not only can orthotropic elastic constants be evaluated, but also, in future work, the generated 3D RVEs may be used to predict the onset and evolution of local damage and cracking in different inclusion-reinforced bio-inspired composites as well as local nonlinear or time-dependent behavior. Furthermore, these micromechanical models can be an applicable and efficacious tool in designing a variety of new composite material systems and optimizing their microstructures.

5.   Conclusions

A new robust micromechanical computational tool for assessing the response of bio-inspired composite materials with high inclusion volume fractions and complex microstructures was proposed. A novel and effective algorithm named staggered hard-core algorithm (SHCA) was developed for rapidly generating realistic three-dimensional periodic staggered and aligned non-uniformly dispersed multi-inclusion representative volume elements (RVEs) for bio-inspired composites reinforced by different types and sizes of inclusions (i.e., hexagonal and cylindrical), which is challenging at best with existing algorithms or commercial software. The spatial non-

uniformity of the RVE inclusions, and thus the accuracy of microstructural representation, was assessed using 3D autocorrelation analysis. The resulting 3D RVE geometries were implemented in the commercial finite element software ABAQUS for micromechanical assessment using customized PYTHON scripts. Volume-averaged orthotropic elastic properties were subsequently computed and compared with available experimental data and well-known analytical models, revealing good correlation for low inclusion volume fractions. However, the analytical model predictions diverge from those of the 3D RVEs for increasing inclusion volume fraction and aspect ratio for both material systems studied, revealing that computational models with accurate depiction of the inclusion geometry, size and spatial dispersion (and thus the inter-inclusion constraining effects) are required for accurately assessing the response of the studied bio-inspired composites. These findings are consistent with those from previously reported studies. Although deemed true for all high inclusion volume fraction bio-inspired composites, this was particularly the case for composites with cylindrical inclusions where a 3D assessment in lieu of a reduced 2D plane strain assessment is necessary for accurate microstructural representation. Furthermore, a comparative study of orthotropic elastic constants was performed for the cylindrical and hexagonal inclusion composites studied. A distinct response to varying inclusion volume fractions and aspect ratios was revealed for each material system, providing insight for future material system design efforts. Furthermore, the proposed computational tool may be an efficient plug-in for commercial FE software ABAQUS to assess the mechanical properties of bio-inspired composites, and in the future may be used for predicting and better understanding their failure characteristics.

Acknowledgements

Data Availability

The raw/processed data required to reproduce these findings cannot be shared at this time as the data also forms part of an ongoing study.

References

[1] Wegst UGK, Bai H, Saiz E, Tomsia AP, Ritchie RO. Bioinspired structural materials. Nat Mater 2015;14:23–36.

[2] Ferrand H Le, Bouville F, Niebel TP, Studart AR. heterogeneous composites 2015;14.

[3] Studart R. Chem Soc Rev Additive manufacturing of biologically- inspired materials 2016:359–76.

[4] Studart AR, Erb RM, Libanori R. Bioinspired Hierarchical Composites. 2015.

[5] Sharp EL, Al-Shehri H, Horozov TS, Stoyanov SD, Paunov VN. Adsorption of shape-anisotropic and porous particles at the air-water and the decane-water interface studied by the gel trapping technique. RSC Adv 2014;4:2205–13.

[6] Wei M, Zhi D, Brandon DG. Microstructure and texture evolution in gel-cast α-alumina/alumina platelet ceramic composites. Scr Mater 2005;53:1327–32.

[7] Compton BG, Lewis JA. 3D-printing of lightweight cellular composites. Adv Mater 2014;26:5930–5.

[8] Barthelat F. Journal of the Mechanics and Physics of Solids Designing nacre-like materials for simultaneous stiffness , strength and toughness : Optimum materials , composition , microstructure and size. J Mech Phys Solids 2014;73:22–37.

[9] Zhang ZQ, Liu B, Huang Y, Hwang KC, Gao H. Journal of the Mechanics and Physics of Solids Mechanical properties of unidirectional nanocomposites with non-uniformly or randomly staggered platelet distribution. J Mech Phys Solids 2010;58:1646–60.

[10] Begley MR, Philips NR, Compton BG, Wilbrink D V, Ritchie RO, Utz M. Journal of the Mechanics and Physics of Solids Micromechanical models to guide the development of synthetic " brick and mortar " composites. J Mech Phys Solids 2012;60:1545–60.

[11] Mirkhalaf M, Barthelat F. Nacre-like materials using a simple doctor blading technique : Fabrication , testing and modeling. J Mech Behav Biomed Mater 2016;56:23–33.

[12] Mirkhalaf M, Ashrafi B. A numerical study on improving the specific properties of

staggered composites by incorporating voids. Mater Today Commun 2017;13:144–54.

[13] Chintapalli RK, Breton S, Dastjerdi AK, Barthelat F. Acta Biomaterialia Strain rate hardening : A hidden but critical mechanism for biological composites ? Acta Biomater 2014;10:5064–73.

[14] Bekah S, Rabiei R, Barthelat F. The Micromechanics of Biological and Biomimetic Staggered Composites. J Bionic Eng 2012;9:446–56.

[15] Dai G, Jr LM. Graphene reinforced nanocomposites : 3D simulation of damage and fracture. Comput Mater Sci 2014;95:684–92.

[16] Abedini A, Butcher C, Chen ZT. Numerical simulation of the influence of particle clustering on tensile behavior of particle-reinforced composites. Comput Mater Sci 2013;73:15–23.

[17] Wang R, Zhang L, Hu D, Liu C, Shen X, Cho C, et al. A novel approach to impose periodic boundary condition on braided composite RVE model based on RPIM. Compos Struct 2017;163:77–88.

[18] Sohn D. Periodic mesh generation and homogenization of inclusion-reinforced composites using an element-carving technique with local mesh refinement. Compos Struct 2018;185:65–80.

[19] Chen Q, Wang G, Chen X, Geng J. Finite-volume homogenization of elastic/viscoelastic periodic materials. Compos Struct 2017;182:457–70.

[20] Li G, Sharifpour F, Bahmani A, Montesano J. A new approach to rapidly generate random periodic representative volume elements for microstructural assessment of high volume fraction composites. Mater Des 2018;150.

[21] Tian W, Qi L, Zhou J, Liang J, Ma Y. Representative volume element for composites reinforced by spatially randomly distributed discontinuous fibers and its applications. Compos Struct 2015;131:366–73.

[22] Datoo M. Mechanics of Fibrous Composites 1991:620.

[23] Yang S, Tewari A, Gokhale AM. Modeling of non-uniform spatial arrangement of fibers in a ceramic matrix composite. Acta Mater 1997;45:3059–69.

[24] Melro AR, Camanho PP, Pinho ST. Generation of random distribution of fibres in long-fibre reinforced composites. Compos Sci Technol 2008;68:2092–102.

[25] Romanov V, Lomov S V., Swolfs Y, Orlova S, Gorbatikh L, Verpoest I. Statistical analysis of real and simulated fibre arrangements in unidirectional composites. Compos Sci Technol 2013;87:126–34.

[26] Jodrey WS, Tory EM. Computer simulation of close random packing of equal spheres. Phys Rev A 1985;32:2347–51.

[27] Yang L, Yan Y, Ran Z, Liu Y. A new method for generating random fibre distributions for fibre reinforced composites. Compos Sci Technol 2013;76:14–20.

[28] Buryachenko VA, Kim RY, Pagano NJ, Spowart JE. Quantitative description and numerical simulation of random microstructures of composites and their effective elastic moduli. Int J Solids Struct 2003;40:47–72.

[29] Vaughan TJ, McCarthy CT. A combined experimental-numerical approach for generating statistically equivalent fibre distributions for high strength laminated composite materials. Compos Sci Technol 2010;70:291–7.

[30] Wang W, Dai Y, Zhang C, Gao X, Zhao M. Micromechanical Modeling of Fiber-Reinforced Composites with Statistically Equivalent Random Fiber Distribution. Materials (Basel) 2016;9:1–14.

[31] Zhang T YY. A comparison between random model and periodic model for fiber-reinforced composites based on a new method for generating fiber distributions. Polym Compos 2017;38:77–86.

[32] Park S-M, Lim JH, Seong MR, Sohn D-W. Efficient generator of random fiber distribution with diverse volume fractions by random fiber removal. Compos Part B 2018.

[33] Ahmadian H, Liang B, Soghrati S. An integrated computational framework for simulating the failure response of carbon fiber reinforced polymer composites. Comput Mech 2017;60:1033-55.

[34] Riaño L, Joliff Y. An Abaqus™ plug-in for the geometry generation of Representative Volume Elements with randomly distributed fibers and interphases. Compos Struct 2019;209:644-51.

[35] Jiménez FL. On the isotropy of randomly generated representative volume elements for fiber-reinforced elastomers. Compos Part B 2016;87:33-9.

[36] Ali D, Sen S. Finite element analysis of the effect of boron nitride nanotubes in beta tricalcium phosphate and hydroxyapatite elastic modulus using the RVE model. Compos Part B 2016;90:336-40.

[37] Bahmani A, Li G, Willett TL, Montesano J. Three-dimensional microscopic assessment of randomly distributed representative volume elements for high fiber volume fraction unidirectional composites. Compos Struct 2018;192.

[38] Journal S, Statistical R, Series S, Statistics CA. Analysis of a Three-Dimensional Point Pattern with Replication Author (s): A . J . Baddeley , R . A . Moyeed , C . V . Howard and A . Boyde Published by : Wiley for the Royal Statistical Society Stable URL : http://www.jstor.org/stable/2986181 Analysis of a Three-dimensional Point Pattern with Replication 2018;42:641–68.

[39] Fabert V, Gunzburger M. Centroidal Voronoi Tessellations : Applications and Algorithms Author (s): Qiang Du , Vance Faber and Max Gunzburger Published by : Society for Industrial and Applied Mathematics Stable URL : http://www.jstor.org/stable/2653198 REFERENCES Linked referen 2017;41:637–76.

[40] Eglen SJ, Lofgreen DD, Raven MA, Reese BE. Analysis of spatial relationships in three dimensions : tools for the study of nerve cell patterning 2008;7:1–7.

[41] Rodieck RW. The density recovery profile : A method for analysis of points in the plane applicable to retinal studies 2018:5238.

[42] Li S, Wongsto A. Unit cells for micromechanical analyses of particle-reinforced composites. Mechanics of materials. 2004;36:543-72.

[43] Li S. Boundary conditions for unit cells from periodic microstructures and their implications. Composites Science and Technology. 2008;68:1962-74.

[44] Fu S-Y, Lauke B, Mäder E, Yue C-Y, Hu X. Tensile properties of short-glass-fiber-and short-carbon-fiber-reinforced polypropylene composites. Compos Part A 2000;31:1117-25.

[45] Jansson S. Homogenized nonlinear constitutive properties and local stress concentrations for composites with periodic internal structure. Int J Solids Struct 1992;29:2181–200.

[46] Sokołowski D, Kamiński M. Homogenization of carbon/polymer composites with anisotropic distribution of particles and stochastic interface defects. Acta Mechanica. 2018;229:3727-65.

[47] Akbarzadeh AH, Abedini A, Chen ZT. Effect of micromechanical models on structural responses of functionally graded plates. Compos Struct 2015;119:598–609.

[48] Abedini A, Chen ZT. A micromechanical model of particle-reinforced metal matrix composites considering particle size and damage. Comput Mater Sci 2014;85:200–5.

[49] Mortazavian S, Fatemi A. Composites : Part B Effects of fiber orientation and anisotropy on tensile strength and elastic modulus of short fiber reinforced polymer composites. Compos Part B 2015;72:116–29.